Biophys Rev (2011) 3:155–169
DOI 10.1007/s12551-011-0054-7

REVIEW

Optical coherence tomography: fundamental principles, instrumental designs and biomedical applications

Dan P. Popescu · Lin-P'ing Choo-Smith · Costel Flueraru · Youxin Mao · Shoude Chang · John Disano · Sherif Sherif · Michael G. Sowa

Received: 29 June 2011 / Accepted: 8 July 2011 / Published online: 6 August 2011

Abstract The advances made in the last two decades in interference technologies, optical instrumentation, catheter technology, optical detectors, speed of data acquisition and processing as well as light sources have facilitated the transformation of optical coherence tomography from an optical method used mainly in research laboratories into a valuable tool applied in various areas of medicine and health sciences. This review paper highlights the place occupied by optical coherence tomography in relation to other imaging methods that are used in medical and life science areas such as ophthalmology, cardiology, dentistry and gastrointestinal endoscopy. Together with the basic principles that lay behind the imaging method itself, this review provides a summary of the functional differences between time-domain, spectral-domain and full-field optical coherence tomography, a presentation of specific methods for processing the data acquired by these systems, an introduction to the noise sources that plague the detected signal and the progress made in optical coherence tomography catheter technology over the last decade.

D. P. Popescu (✉) · L.-P. Choo-Smith · M. G. Sowa
National Research Council of Canada,
Institute for Biodiagnostics,
435 Ellice Avenue,
Winnipeg, MB, Canada R3B 1Y6
e-mail: dan.popescu@nrc-cnrc.gc.ca

C. Flueraru · Y. Mao · S. Chang · J. Disano
National Research Council of Canada,
Institute for Microstructural Sciences,
1200 Montreal Road,
Ottawa, ON, Canada K1A 0R6

S. Sherif
Electrical and Computer Engineering,
University of Manitoba,
75A Chancellor Drive,
Winnipeg, MB, Canada R3T 5V6

Keywords Optical coherence tomography · Biomedical applications · Signal noise · Time-domain · Fourier-domain · Full-field system · Catheter technology

Introduction

In the last decades, new medical imaging technologies have radically improved not only the diagnosis and clinical management of various diseases but have also provided new opportunities for understanding the pathogenesis of various diseases and for the advancement of novel therapies and interventions. The impact in medicine of three-dimensional imaging technologies such as magnetic resonance imaging (MRI), functional magnetic resonance imaging (fMRI), X-ray computed tomography, radioisotope imaging (PET and SPECT), ultrasound and diffuse optical tomography cannot be over-emphasized. Despite their successes and further technical developments, these techniques are limited and for many applications negatively impacted by low spatial resolution; under the best circumstances, the smallest details observable are in the range of half a millimeter. Meanwhile, optical imaging methods such as conventional and confocal microscopy, fluorescence and multi-photon imaging have spatial resolutions of micrometers or better but cannot penetrate deep under the surface of biological samples.

Optical coherence tomography (OCT), a light interference-based optical technique, allows three-dimensional cross-sectional imaging within biological samples with a spatial resolution of 10 μm or less. OCT lies between the deep and the superficial imaging techniques conveying high spatial resolution at imaging depths of millimeters into tissue. Since its conception, in the late 1980s, OCT was developed as a technique enabling high-resolution, real-time and in-situ imaging of tissue microstructure without the need for tissue

excision and processing. As shown in Fig. 1, when comparing imaging methods by their resolutions and imaging depths in tissues, OCT fills a niche located between optical microscopy methods (such as confocal and fluorescence) and ultrasound imaging.

The technological advances made in the last two decades in regard to interference technologies, optical instrumentation, detectors, speed of data acquisition and processing as well as light sources have facilitated the application of OCT technology in a variety of medical fields such as developmental biology, ophthalmology, interventional cardiology, dentistry, gastrointestinal endoscopy, dermatology, laryngology, gynecology, etc. This past decade has seen OCT evolving from an optical imaging method used mostly in research laboratories into a valuable tool used in various areas of medicine and health sciences. This trend is likely to continue as medical applications that exploit the speed, resolving power and convenience of OCT imaging emerge.

Driven by expanding sales in ophthalmology and by new medical applications, the global OCT market is expected to grow to more than US$800 million by 2014 at an annual growth rate of about 21%. Ophthalmology is expected to remain the dominant application for OCT but the growth during the next two to three years will also be driven by applications in cardiovascular medicine, dentistry, gastrointestinal imaging, dermatology, glucose monitoring, and tissue engineering (Smolka 2008; Strategies Unlimited 2010).

Optical coherence tomography: basic principles

OCT is an optical imaging modality that is used to perform high resolution, cross-sectional imaging of internal microstructures in materials and biological systems by measuring the echo time delay and magnitude of backscattered light. In this respect, OCT is somehow analogous to ultrasound imaging, with the provision that image resolutions of 1–15 μm can be achieved in the OCT case, spatial resolutions that are one to two orders of magnitude finer than the ones achieved through conventional ultrasound.

The functional principle behind OCT imaging is light interference. Therefore, a light interference setup is at the core of any OCT system. Although there are many types of interference configurations, as will be described in a later section, the optical fiber-based Michelson setup shown in Fig. 2 will be used to demonstrate the basic concepts of light interference and its role in OCT imaging.

In an OCT system, the light from a low-coherence source is split into two paths by a coupler directing it along two different arms of an interferometer. One arm is designated as the reference arm, while the other is the sample arm. When the light exits the fiber end of either arm, it is shaped by various optical components (mirrors, lenses, etc.) to control specific beam parameters such as shape, depth of focus and the intensity distribution of the light. In the reference arm, the light is back-reflected by a reference mirror and it returns into the interference system, propagating along the same path it came from but in the opposite direction. The same process happens with the light in the sample arm the only difference being that the beam is backscattered by the sample. In an inhomogeneous sample, different structures within the sample will have different indices of refraction and light will be backscattered when it encounters an interface between materials of different refractive index. The returning light from both arms recombine at the coupler and generate an interference pattern, which is recorded by the detector.

For a particular position of the reference mirror, the light propagating in the reference arm travels a certain optical distance and forms the corresponding interference pattern

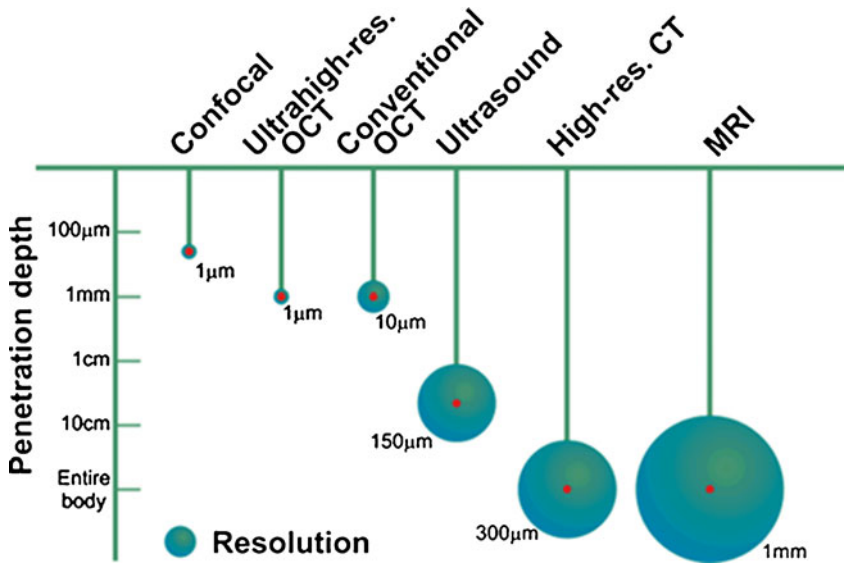

Fig. 1 Comparison of various imaging methods according to their resolutions and penetration depths. The length of the "pendulum" represents the penetration depth while the diameter of the circle represents the spatial resolution of the imaging method. (Adapted by permission from http://obel.ee.uwa.edu.au/research/oct/intro/, the website of the Optical and Biomedical Engineering Laboratory, University of Western Australia)

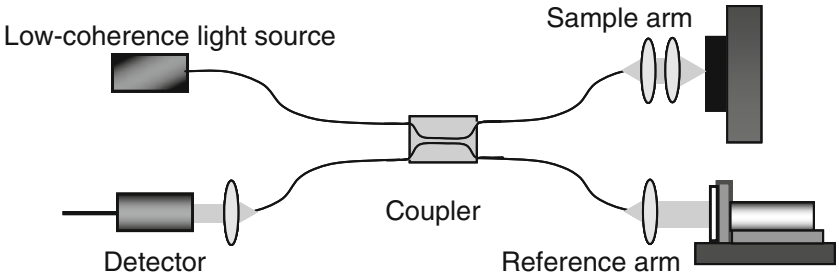

Fig. 2 Fiber-based OCT system in a Michelson configuration. The light from a low-coherence source is split in two by the coupler with each part traveling along a separate arm of the interferometer, the reference and the sample arm. The light backscattered from the reference mirror and from the sample recombine at the coupler and generate an interference pattern, which is recorded by a single point detector

only with light that traveled the same optical distance along the sample arm, including the portion of the distance traveled inside the sample. Therefore, when the reference mirror is translated along the propagation direction of light, for different positions of the mirror, the returning reference generates interference patterns with light backscattered from corresponding depths within the sample. In this way, the dependence on depth of the intensity of light backscattered from beneath the sample surface can be measured.

The OCT signal recorded by the detector during a complete travel of the reference mirror is called a depth scan or an A-scan. In order to form an OCT image, the sample beam has to be translated across the sample surface with an A-scan being recorded at each position of the beam. Therefore, a set of consecutive A-scans is obtained forming an OCT image or otherwise called a B-scan. An example of an OCT image is provided in Fig. 3, which shows a portion about 3 mm wide on the tactile side of a finger. The image (B-scan) contains 600 depth scans (A-scans) with a distance of 5 μm between adjacent scans. The maximum possible depth that can be probed by an OCT system generally depends on the sample itself. The image taken of the finger had a maximum depth of about 1.5 mm. The multi-layered structure of skin at the finger tip can be clearly visualized and the image also has the spatial resolution necessary to detect the sweat glands emerging to the skin surface after passing through epidermis.

A photograph of the probe head of a fiber-based OCT system is shown in Fig. 4 during the acquisition of an ex-vivo OCT image (B-scan). The end of the reference arm has an ultra-small probe lens with forward view attached and is covered with a transparent plastic shield for protection. Partially, the sample arm can be seen in the figure as a yellow portion of optical fiber inside the protective shield. The sample shown in the picture was harvested from the left descending artery of a rabbit specimen that develops spontaneous myocardial infarction. Rich fatty deposits can be easily observed on the exposed luminal side. This variant species was obtained by selective breeding of coronary atherosclerosis–prone Watanabe heritable hyperlipidemic (WHHL-MI) rabbits (Shiome et al. 2003). The arterial piece was cut open along the direction of blood flow and it is exposed with the lumen side facing the OCT probing beam. A vertical balancing motion of the OCT probe head ensures the acquisition of an OCT image which corresponds to a width on the sample surface of 3 mm.

The typical light source in an OCT system is a low-coherence semiconductor super-luminescent diode (SLD). The characteristics of the SLD are an important design parameter since the axial resolution, also known as the

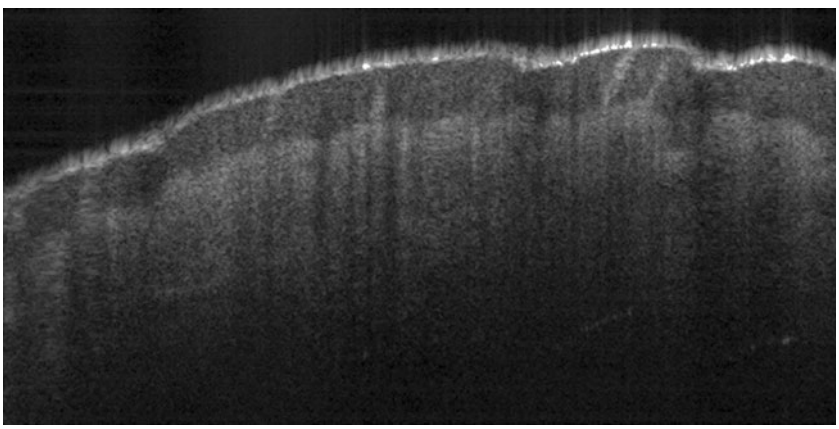

Fig. 3 OCT image of a 3-mm-wide section of the tactile portion of a finger. The multi-layered structure of the skin is imaged to a depth of 1.5 mm below the surface. Sweat glands can be seen running from the dermis to the skin surface while passing through epidermis

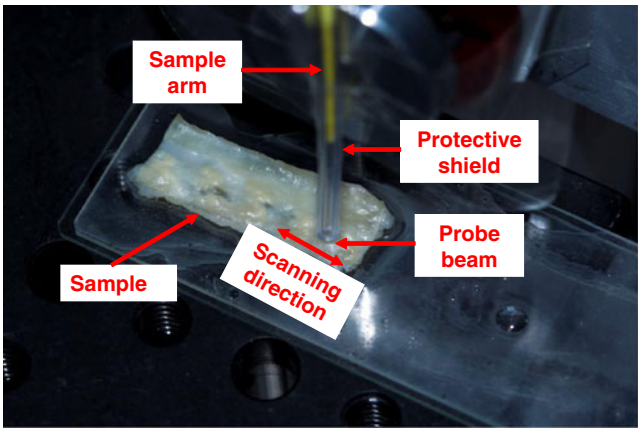

Fig. 4 The probe head ended with an ultra-small ball lens used for forward view is acquiring OCT data from the lumen surface of a WHHL-MI rabbit left descending arterial tissue. Rich fatty tissues can be easily observed on the luminal side

depth resolution or the coherence gate, is the coherence length of the source, an intrinsic parameter of the source which is inversely proportional to its spectral bandwidth. When the spectral distribution of the SLD is Gaussian, the axial resolution Δz is given as:

$$\Delta z = \left(2\ln\frac{2}{\pi}\right)\left(\frac{\lambda^2}{\Delta\lambda}\right) \quad (1)$$

where λ and Δλ are the SLD central wavelength and its bandwidth. Therefore, broadband optical sources are required in order to achieve high axial resolution. Axial resolutions in the micron and sub-micron range can be achieved by using sources with very large spectral band such as femto-second pulsed lasers or white-light sources such as halogen lamps.

The axial and transverse resolutions are independent in OCT imaging. The transverse resolution is determined by the minimum spot size of the focused probing beam, a parameter which is inversely proportional to the numerical aperture (NA) of the focusing lens:

$$\Delta x = \frac{4\lambda}{\pi}\left(\frac{f}{d}\right) = 1.27\frac{\lambda}{NA} \quad (2)$$

In relation (2), *d* is the spot size of the probing beam as it is projected on the objective lens and *f* is the focal length of the objective lens, i.e. the lens or lens system located at the end of the sample arm. An important detail that needs mentioning is that there is a trade-off between transverse resolution and depth of field. A high numerical aperture features a great focusing power translating into excellent transverse resolution, i.e. small diameter of the focused beam, with a corresponding short depth of field. Meanwhile, a low *NA* offers a greater diameter of the beam at the focal point but a large depth of field. Most OCT imaging is performed with a low *NA* lens in order to ensure a depth of field of the order of millimetres, much longer than the coherence length of the source. Commercial OCT systems typically use transverse resolutions of 20–25 μm.

Optical coherence tomography systems

In the point-scanning/point-detection technology, as described above, there are two main OCT technologies, time-domain OCT (TD-OCT) and Fourier-domain OCT (FD-OCT). Fourier-domain OCT imaging can also be done in two ways: by spectral-domain OCT (SD-OCT) and by swept-source OCT (SS-OCT). Direct acquisition of 2D OCT images is accomplished through another method, full-field OCT (FF-OCT).

TD-OCT is based on a detection technique that uses a low-coherent light source and a scanning reference delay. Most of the principles and parameters that define this OCT imaging method were introduced in the previous section on basic principles. The light source, usually a low-coherence SLD or pulsed laser, is split into two paths by an optical splitter. The light from one path is back-reflected from a reference mirror that is on a controlled translation motion, allowing the reference light to travel a known path length and to undergo a measurable variable time delay. The light from the second path is directed onto the sample and is backscattered by its internal structure producing interference patterns with the reference light that traveled an equal optical distance, thus providing the depth information and the locations of various structures from within the sample. TD-OCT was the first OCT technology developed, appearing in the1990s. The theory, technical details and applications of TD-OCT have been extensively reported and can be found in references published during that period (Schmitt et al. 1994; Izzat et al. 1994; Pan et al. 1995; Fercher 1996; Dolin 1998; Podoleanu and Jackson 1999; Schmitt 1999).

While in a TD-OCT measurement the light echoes are detected sequentially by the step-movement of a reference mirror, in FD-OCT the light echoes come at the same time from all axial depths and are detected as modulations in the source spectrum with all the spectral components captured simultaneously (Fercher et al. 1995; Hausler and Lindner 1998). The main difference between these two technologies is that the reference arm in an FD-OCT system has a static mirror instead of a moving one as in TD-OCT. This feature eliminates the moving mirror and the limitations imposed by the inertia of that mechanical device. Due to the elimination of the mechanical translation, FD-OCT systems are capable of higher data acquisition speeds compared to TD-OCT systems. The instantaneous current generated in an FD-OCT detection system by incoming light is a function dependent on the source wavelength (or the wavenumber) sampled at that instant. The acquired wavenumber-dependent data is

transformed into axial scan information (i.e. the A-scan or the signal dependence on depth as it was defined in the previous section) by performing an inverse Fourier transform. Driven by advances in both detection and source technologies, FD-OCT has evolved into two primary methods, SD-OCT and SS-OCT.

The core of an SD-OCT is also a Michelson-type interferometer with a stationary reference mirror, but, instead of the interference signal being captured by a point detector, after the two returning beams recombine and form the interference pattern at the beam splitter, their spectrum is spread out or dispersed with a diffraction grating and detected by a high-speed CCD line camera. A Fourier transform is performed on the spectrally-resolved interference pattern detected by the camera array thus obtaining the reflectivity as a function of depth, i.e. the A-scan. The acquisition speed of such systems is limited by the read-out rate of the line sensor, which is routinely in the kHz range (Fercher et al. 1995; Hausler and Lindner 1998; Wojtowski et al. 2002).

Unlike SD-OCT where the interference pattern is dispersed immediately before detection, SS-OCT uses a broadband source that scans in a controlled way a laser with a narrow spectral line across the available bandwidth of the source. As before, the reference beam is reflected from a fixed mirror and forms an interference pattern with the light backscattered by the sample that is subsequently detected by a point detector. Point detection is one advantage that SS-OCT has over SD-OCT because of its higher signal-to-noise ratio when compared to area or line detectors. Because of the way the source laser is scanned across the available broadband in SS-OCT, the output is a wavenumber-dependent photo-current that is recorded by the point detector simultaneously with the scanning of the narrow-band laser (Chinn et al. 1997; Golubovic et al. 1997; Lexer et al. 1997). The quantity of interest, the depth profile or A-scan, is also obtained by performing the Fourier-transform of the detected signal over one sweep of the laser across the available broadband. Since the light from a swept-source consists of a laser signal with a continuously changing wavelength over time, the coherence length of the scanned laser determines the maximum imaging depth of the system while the wavelength range over which the laser is swept determines the axial resolution of the system. Therefore, a scanning laser with a narrow linewidth enables a deeper probing depth while a wider sweep range produces OCT images with higher axial resolution.

The data acquisition speed for a typical Fourier domain device is usually 45–100 times faster than for TD-OCT. It is possible now to capture 18,000–40,000 A-scans per second since the spectral data is acquired simultaneously (Murphy 2008). Fast acquisition of a large number of scans allows 3D reconstructions that could be further manipulated to better visualize specific tissue structures. Additionally, when the acquisition speed is high there are less movement artefacts when in vivo OCT imaging is performed. Another advantage in addition to higher acquisition speed is that the signal-to-noise ratio (SNR) for FD-OCT is significantly better than the TD-OCT SNR. It has been determined that FD-OCT has a sensitivity advantage of 20–30 dB compared to TD-OCT (Choma et al. 2003; Wang et al. 2009).

While the OCT methods previously described interrogate, by using a focused beam, a single point on the sample at a time and build a volumetric imaging by recording an array of A-scans, another OCT technique, called full-field OCT (FF-OCT), produces tomographic images in an *en face* orientation. These images are perpendicular to the optical axis of the sample arm and are acquired in one shot, without raster-scanning the probe beam across the sample surface. In FF-OCT (sometimes also named full-field optical coherence microscopy), the entire field is illuminated with a low coherence light source, usually a white-light source such as a halogen lamp (Vabre et al. 2002; Dubois 2004). The spectral properties of the light source confer FF-OCT an axial resolution of about 1 μm and a transverse spatial resolution similar to that of conventional microscopy (also ~1 μm). The tomographic images are generated by combining *en face* interference patterns corresponding to different depths within the sample and recorded by an area detector such as a 2D charge-coupled device (CCD) or complementary metal-oxide-semiconductor (CMOS) camera. The experimental design of an FF-OCT system contains the light source, detector, sample and reference mirror arranged in a free-space Michelson interferometer design. There are identical microscope objectives positioned in the sample and reference arms of the interferometer, a configuration which is referred as a Linnik interferometer (Dubois et al. 2002; Kino and Chim 1990). In FF-OCT, it is necessary to record two or more phase-displaced *en face* interference patterns in order to obtain a tomographic image corresponding to a sample slice located at a specific distance underneath the surface. The phase shift is accomplished by displacing the reference mirror with a high resolution piezoelectric translation stage. Several algorithms used for extracting FF-OCT images from phase-displaced interference patterns are presented at the end of the next section.

Algorithms for signal processing in optical coherence tomography

The detected signal generated by a monochromatic coherent light source, i.e. a continuous-wave laser, at the output of an OCT interferometer can be expressed as:,

$$I_d = E_s^2 + E_r^2 + 2E_sE_r\cos(2\,\Delta L/\lambda_0), \tag{3}$$

where, λ_0 is the laser wavelength, ΔL is the optical path difference between the sample and the reference arms,

while E_s and E_r are the optical electric fields incoming from the sample and the reference arm, respectively. When, instead of monochromatic coherent source, a low coherence light source with a Gaussian spectral distribution is used in the interferometer, the detected signal becomes:

$$I_d = E_s^2 + E_r^2 + 2E_sE_r \exp\left(-4\ln 2(\Delta L/L_c)^2\right)\cos(\omega_0 \Delta L) \quad (4)$$

In Eq. (4), $\exp\left(-4\ln 2(\Delta L/L_c)^2\right)\cos(\omega_0 \Delta L)$ is called the coherence function, with ω_0 being the optical wavenumber corresponding to the central wavelength λ_0 while L_c is the coherence length of the Gaussian source.

In the case of data acquired by a time-domain OCT system, considering E_r a constant reference signal normalized to unity, Eq. (4) becomes:

$$I_d = I_0 + A \times G(\Delta L)\cos(\omega_0 \Delta L) \quad (5)$$

where, $I_0 = E_s^2 + E_r^2$ represents the background DC bias, A is the amplitude of backscattered signal, G(ΔL) is the Gaussian gate function, and *cos( )* term represents the fast-varying wavelength carrier signal. Such an OCT system yields a maximum of the received signal when ΔL=0, i.e., the optical lengths are identical between the reference and sample arms. There are two processing steps needed in order to obtain the OCT image from the detected time-domain signal: (1) remove the DC part and (2) extract the maximal value of envelope of *cos( )* item by low-pass filtering while also eliminating the fast-varying interference fringes.

From the point of view of mathematical formalism, the translation of the reference mirror along the optical axis used in TD-OCT produces a signal that can be expressed as a convolution between the electrical component of the optical field in the sample arm and the electrical component from the sample arm. Therefore, the detected current is proportional to the value of this convolution function:

$$I_d \sim E_s \otimes E_r \quad (6)$$

If a Fourier transform is applied to this convolution function, then the dependence on the frequency of the detected signal is obtained as:

$$\begin{aligned} I_d(\omega) &= [s_r(\omega) + s_s(\omega)] \times [s_r(\omega) + s_s(\omega)]^* = \\ &= [s(\omega) + H(\omega)s(\omega)] \times [s(\omega) + H(\omega)s(\omega)]^* = \\ &= \tfrac{1}{4}P(\omega) + \tfrac{1}{4}P(\omega)|H(\omega)|^2 + 2\mathrm{Re}[H(\omega)] \end{aligned} \quad (7)$$

where $s_r(\omega) = s_s(\omega) = 1/2\ s(\omega)$ and $P(\omega) = s^2(\omega)$ represents the power spectrum of the light source. Also, $H(\omega)$ is the spectrum of point-spread-function (PSF) of the sample while Re[ ] denotes the real part. Equation (7) is the foundation of signal processing in Fourier-domain OCT imaging (Leitgeb et al. 2003; Chinn et al. 1997). The first and second terms from the right-hand side of (7) are considered the DC component, and need to be removed. The third term contains the tomography information and the necessary algorithm to extract it in order to obtain the final OCT image is given by:

$$h(z) = \log(Trunc\{IFT[I_d(\omega)]\}) \quad (8)$$

In Eq. (8), $h(z)$ is the reconstructed OCT image, *Trunc*{ } represents the Truncation function used for trimming out the DC component, *log*( ) is the $\log_{10}$ function and IFT is the inverse Fourier transform.

For a full-field OCT (FF-OCT) system, whose detection system contains an area detector, the previous equations, which all pertain to point detectors, should be extended to the (x, y) 2D plane, i.e. the plane perpendicular on the propagation direction of the sample beam. Caution has to be exercised since there are two types of interferences occurring in the data acquired by FF-OCT. One is the temporal interference generated because of the displacement of the reference mirror. This signal is acquired by each pixel of the FF-OCT area detector and it is similar to the signal generated by a TD-OCT in a point detector. Another type of signal, which is characteristic only to FF-OCT, is the spatial 2D pattern obtained due to interference at the detector site of various phase fronts coming from across the surface of the sample or from the optical components of the instrument. The previously described algorithms provide the means to only remove the temporal pattern, i.e. the fringes generated by the translation of the reference mirror. In order to obtain a good FF-OCT image, the fringes resulting from lateral 2D interference also need to be removed.

In the case of balanced optical paths between the reference and sample arms, i.e. ΔL=0, the 2D detected FF-OCT signal is reduced to the following expression:

$$I_d(x,y) = I_0(x,y) + A_i(x,y) \times \cos[\phi_i(x,y)] \quad (9)$$

In this formula, $A_i(x,y)$ is the quantity of interest, i.e. the sectional tomography image of the i^{th} layer of the sample, layer located at a distance z_i below the sample surface. To retrieve $A_i(x,y)$, the spatial interference fringe pattern contained within the $\cos[\phi_i(x,y)]$ term, has to be removed together with the background component, $I_0(x, y)$.

Akiba et al. (2003) demonstrate a method for removing the spatial interference term by acquiring two FF-OCT images that are π/2 phase-shifted $I_1(x,y)$, $I_2(x,y)$ together with a background image $I_0(x,y)$. Thus, a final FF-OCT image free of artefacts can be obtained from:

$$A_i(x,y) = \left\{S_1(x,y)^2 + S_2(x,y)^2\right\}^{\frac{1}{2}} \quad (10)$$

with $S_1(x,y) = I_1(x,y) - I_0(x,y)$, and $S_2(x,y) = I_2(x,y) - I_0(x,y)$. The background image $I_0(x,y)$ can be obtained before or after the scanning. The π/2 phase-shifted images $I_1(x,y)$ and

$I_2(x,y)$ can be acquired either by using two "smart pixel" CCD cameras, a method that provides the required phase shift by electronic processing, or by grabbing the images one after the other with the phase shift induced by the controlled translation of the reference mirror. When the phase-shift is an arbitrary value other than π/2, the following formula should be used according to Chang et al. (2005):

$$A_i(x,y) = \left\{ S_1(x,y)^2 + \left[(S_2(x,y) - S_1(x,y)\cos\varphi)/\sin\varphi \right]^2 \right\}^{\frac{1}{2}} \tag{11}$$

However, in both Eq. (10) and (11), there is the need to know the phase-shift a priori in order to extract the FF-OCT image from the acquired data. To solve for the $A_i(x,y)$ without knowing the value of the phase-shift, more equally phase-shifted images have to be acquired. As an example, a 5-step algorithm based on the acquisition of five consecutive phase-shifted images and the consequent use of Hariharan equations was proposed by Greivenkamp and Bruning (1992) and by Novak (2003). The five raw FF-OCT images are acquired as:

$$\begin{aligned} I_1(x,y) &= I_0(x,y) + A_i(x,y)\cos[\phi(x,y) - 2\varphi], \\ I_2(x,y) &= I_0(x,y) + A_i(x,y)\cos[\phi(x,y) - \varphi], \\ I_3(x,y) &= I_0(x,y) + A_i(x,y)\cos[\phi(x,y)], \\ I_4(x,y) &= I_0(x,y) + A_i(x,y)\cos[\phi(x,y) + \varphi], \\ I_5(x,y) &= I_0(x,y) + A_i(x,y)\cos[\phi(x,y) + 2\varphi] \end{aligned} \tag{12}$$

and the tomography image is extracted through the following procedure:

$$A_i(x,y) = \left[\frac{(I_2(x,y) - I_4(x,y))}{2\sin\varphi} + \frac{2I_3(x,y) - I_5(x,y) - I_1(x,y)}{4\sin^2\varphi} \right]^{1/2} \tag{13}$$

The only condition that needs to be fulfilled for this method to work is that φ cannot be an integer number of π radians. As a bonus, the phase itself can also be calculated:

$$\tan\varphi = \frac{2[I_2(x,y) - I_4(x,y)]}{3I_3(x,y) - I_5(x,y) - I_1(x,y)} \tag{14}$$

Because in the 5-step algorithm the calculations described in Eqs. (12), (13) and (14) have to be completed for each pixel of the 2D detector, the computation burden is relatively heavy, particularly for large images. Dubois (2001) proposed a 4-integration buckets algorithm, in which four images with circularly-shifted phase angles of 0, π/2, π, 3π/2 are acquired. Analysed by using Bessel functions of first kind, J_n, the FF-OCT image is extracted through:

$$A_i(x,y) = k \left\{ \begin{matrix} [I_1(x,y) + I_4(x,y) - I_2(x,y) - I_3(x,y)]^2 + \\ [I_1(x,y) - I_4(x,y) - I_2(x,y) + I_3(x,y)]^2 \end{matrix} \right\}^{\frac{1}{2}} \tag{15}$$

with k being a coefficient depending on the Bessel functions J_n.

A more practical and faster version of the 4-bucket algorithm was proposed by S. Chang et al. (2007). Based on a defined energy-type operator (Maragos et al. 1993), the extraction algorithm becomes:

$$A_i(x,y) = \left| \begin{matrix} [I_3(x,y) - 2I_2(x,y) - I_1(x,y)]^2 - [I_2(x,y) - I_1(x,y)] \times \\ [I_4(x,y) - 3I_3(x,y) - 3I_2(x,y) - I_1(x,y)] \end{matrix} \right|^{\frac{1}{2}} \tag{16}$$

Where $I_1(x,y)$, $I_2(x,y)$, $I_3(x,y)$ and $I_4(x,y)$ are four phase shifted images. This algorithm is about three times faster.

Optical detection and noise in optical coherence tomography

Detection in OCT imaging is based on the capture of interference patterns by electronic detectors. Intrinsically, these interference patterns are time and/or spatial distributions of individual photons. At the end, the quality of a recorded OCT image is dependent on the number of individual photons captured by the detector and on the properties of the detector itself.

Every incident photon falling on an electronic detector carries a probability to generate a photoelectron, which results in a short electric current pulse which would represent the detector output corresponding to that incident photon. The probability of a photoelectron generation from an incident photon and the width of the subsequent current pulse depend on the responsivity and bandwidth of the detector, respectively. Therefore, the total photocurrent in the detector, which would be generated by a spatial and/or time distribution of photons, is the sum of space- and/or time-shifted short current pulses resulting by the detection of some photons from the input distribution. As the *photon* is a quantum mechanical concept, it is typical to use a semi-classical approach to treat light detection based on generated photoelectrons instead of incident individual photons (Saleh 1978). Detection of light by an electronic detector involves three main noise sources: shot noise, photon excess noise and electronic noise.

The shot noise, which represents the limiting factor in all light detectors after all other noise sources are eliminated, arises from the quantum nature of photons. When coherent light is incident on a detector, photons are randomly absorbed and the corresponding photoelectrons are generated according to a Poisson probability distribution function. The rate of this Poisson distribution will be *deterministic* and will depend on the intensity of the incident light, i.e. the number of incident photons. Due to the discrete and random nature of the Poisson events (the photoelectrons) physically arising from the quantum nature of photons, the total photoelectric current read by the

detector will the sum of randomly shifted (in time) short current pulses. The variance of this shot noise is given by

$$\sigma^2_{shot} = 2e\widetilde{I}B \tag{17}$$

where e is the electronic charge, $\widetilde{I}$ is the mean of the photocurrent and B is the electrical bandwidth of the detector (Saleh 1978).

Meanwhile, when the incident light contains also an incoherent portion, photoelectrons are also generated randomly according to a Poisson probability distribution function. However the rate of this Poisson distribution will be *random* (instead of deterministic as in the case of shot noise) and will depend on the coherence degree of the incident light. This additional randomness in the rate of the Poisson process that governs the generation of photoelectrons results in another noise source called photon excess noise (Saleh 1978).

In the case of *thermal* incoherent light (sometimes powerful halogen lamps are used as light sources in FF-OCT systems), this random-rate Poisson distribution becomes a Bose-Einstein distribution with a variance equal to the variance of the original fixed-rate Poisson distribution (shot noise) plus the extra (photon excess noise) given by

$$\sigma^2_{photon\_excess} = \left(1 + V^2\right)\widetilde{I}^2 B/\Delta\nu, \tag{18}$$

where V and $\Delta\nu$ are the degree of polarization and the effective linewidth of the source, respectively (Morkel et al. 1990).

Another type of noise affecting optical detectors is induced by electronic thermal fluctuations. This noise could be modeled as a white Gaussian noise (WGN) which has a variance given by

$$\sigma^2_{thermal} = \frac{4K_B TB}{R_L} \tag{19}$$

Where K_B is Boltzmann's constant, B is the electrical bandwidth of the detector, and R_L is the equivalent load resistor at temperature T (Oliver 1965). Note that an easy and very often used method to quench the electronic thermal fluctuations is to cool down the detector.

One could think of noise analysis in OCT in two ways: (1) calculation of average signal-to-noise ratios (SNR) to assess the performance of different experimental configurations (Takada 1998; Podoleanu and Jackson 1999; Rollins and Izatt 1999; Podoleanu 2000; Rosa and Podoleanu 2004), or (2) derivation of statistical moments and probability distribution functions to be used for statistical image processing techniques, e.g., minimum mean squared error, maximum likelihood and Bayesian estimation, which are usually more powerful than deterministic methods (Sherif et al. 2008).

A typical time-domain OCT setup with direct optical detection is shown in Fig. 2, a configuration which tends to have a high excess photon noise. In order to quench this excess photon noise, another type of setup is used. Its layout is shown in Fig. 5 and it is called balanced differential optical detection. Although the examples shown are both TD-OCT systems, this discussion is also applicable to frequency-domain OCT setups as well.

For balanced differential detection (also named balanced heterodyne detection), light in the interferometer is equally split into two beams and a phase shift of 180° is introduced between the two interfering optical fields of one of the beams. This is achieved by the combined effect of the two optical couplers shown in Fig. 5, where each coupler introduces a phase shift of 90° between the field at one of its input ports and the field at the non-corresponding output port. After propagating the same optical distance, these beams are detected by two identical but independent detectors whose photocurrents are subtracted to obtain the A-scan. Therefore, balanced differential detection results in a purely interference signal (fringes) without any background signals, which largely eliminates the photon excess noise (Rollins and Izzat 1999). Extended analysis of both first and second order statistics of the depth-scan photocurrent in time-domain optical coherence tomography (TD-OCT) systems using polarized thermal light sources were derived by Sherif et al. (2008) for both direct and differential detection cases.

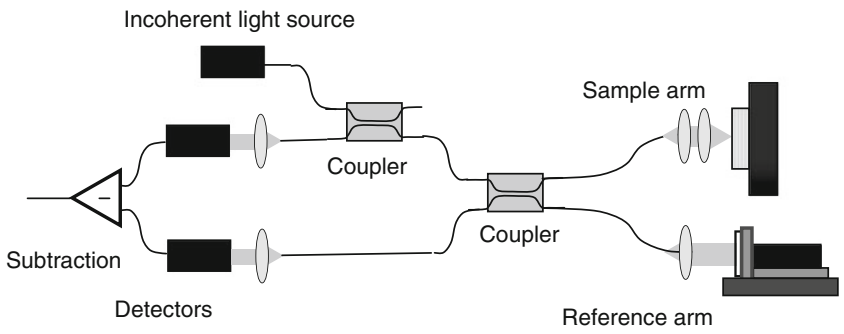

Fig. 5 A typical TD-OCT setup with differential optical detection

After eliminating the other noise sources, the remaining shot-noise limited signal-to-noise ratio in time-domain OCT is calculated by Swanson et al. (1992) as:

$$SNR_{TD-OCT} = \frac{\rho P_s R_s}{2eB}, \quad (20)$$

where ρ is the responsivity of the detector, P_s is the instantaneous optical power incident on the sample, and R_s is reflectance of the sample. We note that the *SNR* of a TD-OCT system is proportional to the responsivity of the detector and to the optical power reflected from the sample, but is independent of the optical power level in the reference arm.

Meanwhile, the shot-noise limited signal-to-noise ratio in frequency-domain OCT is determined by Choma et al. (2003) as:

$$SNR_{FD-OCT} = \frac{M}{2}\frac{\rho P_s[k_m] R_s}{2eB}, \quad (21)$$

with $P_s[k_m]$ being the fraction of instantaneous optical power incident on the sample that corresponds to m^{th} spectral channel of the detection system, and M is the number of detection channels. We note that $SNR_{FD\text{-}OCT}$ is higher than $SNR_{TD\text{-}OCT}$ by a factor of $\frac{M}{2}$. However, this improvement factor is typically reduced by an extra factor of 2 since a practical optical source would not have equal power in all its spectral channels, e.g. a Gaussian spectral shape. Assuming M to be approximately equal to 10^3, a usual order of magnitude for the number of spectral channels (i.e. wavelengths) employed in either SD-OCT or SS-OCT layouts, FD-OCT systems are theoretically capable of about 20 dB higher SNR than TD-OCT systems.

Advances in catheterized optical coherence tomography

In most tissues, OCT has a typical imaging depth limitation of 1–4 mm. Therefore, with the notable exception of ophthalmic OCT, when imaging is performed on internal body structures, such as the cardiovascular system or the gastrointestinal tract, the OCT probe needs to be integrated into a catheter, endoscope, or biopsy needle, arrangement that can bring it close to the structure under investigation. The optics integrated within the probe must be able to focus and scan the OCT beam according to specific parameters and to collect the light backscattered by the sample. OCT catheterized probes are designed to collect images either in the forward scanning (forward-viewing) mode or in the radial outward scanning mode (side-viewing). It is widely recognized that OCT system performance is affected by compactness, scanning speed, and flexibility of the imaging probe (Liu et al. 2004; Tran et al. 2004; Zara and Patterson 2006; Munce et al. 2008; Min et al. 2009).

Optical fiber lens probes, such as graded-index (GRIN) fibers or fiber ball lens, have been proposed (Swanson et al. 2002; Shishkov et al. 2006) and implemented for both forward- and side-viewing applications (Reed et al. 2002; Mao et al. 2007; Mao et al. 2010). The main advantage of fiber lenses over conventional glass lenses are their small size, and ability to auto-align to the optical fiber due to the creation of a low-loss fusion-spliced interface, low back-reflection and high mechanical integrity. In addition, a beam diverter can be easily attached to the fiber lens by either fusion splicing a GRIN fiber lens as in Mao et al. (2007) or by polishing a facet directly onto the surface of a ball fiber lens (Mao et al. 2010). The fiber tip of forward scanning devices can be displaced using various electrostatic or magnetic techniques (Munce et al. 2008; Min et al. 2009). Methods to manipulate the focused beam have been demonstrated with a dual-reflective MEMS mirror and with a pair of angle-cut rotating GRIN lenses (Wu et al. 2006; Wu and Xie 2009).

Various rotating OCT probe drive systems have been developed by industry and the research community due to the numerous applications for a side-viewing probe. With a side scanning probe, the focused light from the distal end of the fiber is redirected radially outward by using an optical prism. The circumferential scan is performed by rotating either the entire optical assembly or by rotating the mirror prism with a micro-motor located at the distal tip of the probe. In early devices, in order to perform an OCT scan of internal structures, a hollow torque cable is rotated while the optical fiber cable is moved longitudinally within a transparent housing. These earlier devices had a relatively large diameter of about 1 mm.

A recent development from Lightlab Imaging (St. Jude Medical), the ImageWire, has a diameter as small as 0.25 mm including the outer plastic sheath. Circumferential scanning is performed by rotating the single-mode fiber in a plastic sheath that is connected to a fiber optic rotary joint. The probing OCT beam is radiated outward from the polished 45° fiber tip (Swanson et al. 2002). Some limitations of this design include: rotating the fiber probe introduces time-varying fiber birefringence; the rotary optical joint introduces optical losses; and rotational motion of the fiber is non-uniform. To resolve the problems introduced by non-uniform rotational distortions, Lightlab has implemented a viscous damping fluid located within the sheath to provide viscous drag during the fiber rotation (Petersen et al. 2005).

In several improved designs, a mirror prism connected to a micro-motor deflects light radially from a stationary optical fiber. These designs eliminate the need to rotate the distal end of the fiber (Herz et al. 2004; Su et al. 2007; Tran et al. 2004). Some of the drawbacks of this design include: the electrical wires obscure a portion of the radial scan;

electrical components in the probe is a potential safety concern; and the probe head may be more difficult to miniaturize.

Another design based on a rigid concentric drive system uses a rotating endoscope, which consists of a stationary central core that includes the fiber and the focusing lens, as well as a rotating inner tube containing a rod prism (Bonnema et al. 2009). The outer diameter of the probe is 2.1 mm. However, its applications are limited to those procedures that require a rigid endoscope.

The feasibility of using an electro-thermally actuated micro-mirror MEMS device for performing circumferential scanning has been demonstrated (Xu et al. 2007). This micro-mirror, mounted 90° with respect to the optical axis of a GRIN lens that terminates the fiber from the OCT sample arm, is capable of angular deflections of up to 45°. This design has the potential to be developed into a more flexible and smaller-diameter probe, but electrical components are still required within the probe.

Rotating probes have been developed with eccentric optics where forward and side imaging is performed in a single rotation (Takahashi et al. 2007). The length of the rigid portion is 10 mm and the outer diameter is 2.6 mm. The dimensions of the rigid portion could be a limitation for situations that require flexibility and small size.

A new design of an in situ on-axis rotary probe has been developed, which features a non-rotating fiber cable (Chang et al. 2010). The optical fiber, which passes through the centre shaft of a micro-motor, remains stationary when the motor is running. A mirror with a 45° reflecting angle is solidly mounted to the motor's rotating shaft. When the mirror rotates, the light exiting the fiber is reflected as a side-view scanning beam. In contrast to existing probes, this novel design can provide a more accurate, uniform and stable measurement. In addition, it yields a much stronger signal with almost no time-varying fiber birefringence.

Recent technology developments in catheter probe design have enhanced the capabilities of OCT for in vivo imaging in gastrointestinal cancers (Standish et al. 2007; Isenberg et al. 2005), cardiovascular disease (Munce et al. 2006, 2008), bladder cancer (Wang et al. 2007), and neurological disorders (Jafri et al. 2005). Needle-based biopsy guidance with OCT is underpinned by the inherent compatibility of OCT with miniature fiber-optic probes (Reed et al. 2002; Iftimia et al. 2005; Yang et al. 2005; Li et al. 2006; Goldberg et al. 2008).

Optical coherence tomography applications

Most of the anatomical components of the eye transmit light with minimal optical attenuation and scattering. This property has made ophthalmic and retinal imaging the first and, to date, the most successful application for OCT. The potential for high resolution OCT imaging of ophthalmic conditions was tested for the first time almost three decades ago (Fercher and Roth 1986; Fujimoto et al. 1986; Fercher et al. 1988) with the acquisition of cross-sectional 2-D images soon to follow (Huang et al. 1991). The first in vivo OCT studies of human retina were performed by Swanson et al. (1993) and by Fercher et al. (1993). In a short time, it has became obvious that no other technology used for ocular imaging comes close to the potential of OCT to produce non-invasive, high-resolution images of human eye and retina. Presently, ophthalmic diagnosis is one of the most clinically developed OCT applications with several systems approved and marketed for clinical use such as the Visante system by Carl Zeiss Meditec (FDA approved in October 2005) and lamp-mounted OCT system by Heidelberg Engineering (FDA approved in March 2006).

OCT technology was first commercialized for ophthalmologic applications and it is now accepted as "the standard of care". It has been estimated that more than 37,000 scans were performed daily in the USA as early as 2006 (Walz 2006). Through the widespread adoption of this technology in ophthalmology, global sales of OCT equipment have grown from less than US$10 million in 2001 to nearly $200 million in 2007. Extrapolating the growth rates from the last 5 years, the ophthalmic equipment market is expected to grow to about $490 million by 2014 (Smolka 2008; Strategies Unlimited 2010). Current applications in ophthalmology, where OCT technology started to be widely used, include examining the retina for age related macular degeneration, diabetic retinopathy, and glaucoma, as well as probing the anterior segment for corneal and refractive power measurements.

Intravascular OCT has also been developed to exploit the high resolution of the imaging method to help direct coronary artery interventions and for the identification of vulnerable plaques (van der Meer et al. 2005; Patel et al. 2005; Regar et al. 2003; Yabushita et al. 2002). Since OCT imaging can be implemented through fiber-based systems it can be easily adapted to the existing coronary catheters Tearney et al. (2003a, b). Specialized catheters designed for circumferential OCT imaging of arterial pathology in in vivo settings were developed by incorporating optical fibers with gradient refraction index and a deflecting prism at one end into commercially available intra-vascular ultrasound catheters (Shiskov et al. 2000).

Ex vivo studies revealed the potential for clinical classification of the different types of plaques based on OCT arterial imaging. The accuracy of OCT for characterizing plaque type has been established by using histopathological diagnostics as the gold standard. This comparison yielded a sensitivity and specificity ranging from 71 to 79% and 97–98% for fibrous plaque, 95–96% and 97% for fibrocalcific plaques, and 90–94% and 90–92% for lipid

rich plaques, respectively (Yabushita et al. 2002). Subsequent work has shown that OCT arterial imaging can provide quantification of macrophage content (Tearney et al. 2003a, b), differentiation between red blood cell-rich and platelet-rich thrombus (Jang et al. 2002), differentiation of thrombus from plaque and arterial wall (Jang and Hursting 2005), identification of multinucleated macrophages (Tearney et al. 2003a, b) and cholesterol crystals (Tearney et al. 2003a, b).

An ex-vivo OCT image of a fatty portion (similar to the ones observed in Fig. 4) located on the luminal side of a WHHL-MI rabbit artery is displayed as an example in Fig. 6. The image is 3 mm wide, 1.5 mm high and is acquired with a swept-source emitting at 1,310 nm with axial and transversal resolutions of 12 and 10 μm, respectively. Atherosclerotic-related structures developed under the luminal surface such as lipid pools, macrophage accumulations and fibrous caps and can be easily observed in this OCT image.

The anatomical arterial features observed in ex vivo samples were replicated in in vivo OCT imaging studies on living human patients at the beginning of this decade (Jang et al. 2001; Jang et al. 2002). Central to the development of OCT technology for interventional coronary artery imaging, algorithms for fast automated identification and segmentation of specific clinical markers and providing for enhanced soft tissue contrast within large sets of OCT data are being developed (Popescu et al. 2010; Flueraru et al. 2010)

From a technique tested only in research laboratories, intravascular OCT has evolved into a tool used for guiding procedures and for assessing vascular conditions during surgical interventions. Recently, at the beginning of May 2010, OCT technology received clearance from the U.S.A. Food and Drug Administration (FDA) to be used for intravascular imaging. Intravascular OCT is currently approved in over 35 countries from Europe and Asia, and it has been used by leading hospitals for high-resolution imaging in thousands of coronary interventions to date. The high number of research publications focused on arterial OCT, and the fact that LightLab (FDA approved) and Volcano are in the process of commercializing products, are strong indicators that cardiovascular medicine will be the next big OCT market to be exploited. Although cardiovascular OCT is not expected to replace intravascular ultrasound (IVUS), in a similar manner that OCT replaced ultrasound in ophthalmology, it has been proven to be a valuable tool for arterial imaging.

In recent years, OCT has been also developed for dental applications such as caries detection and periodontal diseases (Feldchtein et al. 1998; Wang et al. 1999; Fried et al. 2002, 2005; Baumgartner et al. 2000; Amaechi et al. 2001, 2003; Brandenburg et al. 2003; Colston et al. 2000; Ngaotheppitak et al. 2005). These studies have demonstrated the potential of using this technique for in vivo imaging of intra-oral tissues. The OCT images obtained were able to delineate structural components of the gingival tissue (e.g., sulcus, epithelium, connective tissue layer) as well as hard tissue structures (e.g., enamel, dentin, dentino-enamel junction). Some approaches involve improvements in imaging by using polarization-sensitive OCT (PS-OCT) (Baumgartner et al. 2000; Ngaotheppitak et al. 2005; Hitzenberger et al. 2001), a method that takes advantage of the birefringent properties of enamel mineral and allows deeper light penetration (Fried et al. 2002). PS-OCT technology has recently been used to examine caries lesions and has been shown to detect approximal and occlusal caries on extracted teeth. In addition to providing a measure of the intensity of backscattered light as a function of depth, PS-OCT also provides an assessment of the polarization state of the backscattered light relative to depth. If the sample under investigation exhibits birefringence properties, such as tooth enamel, then PS-OCT images may

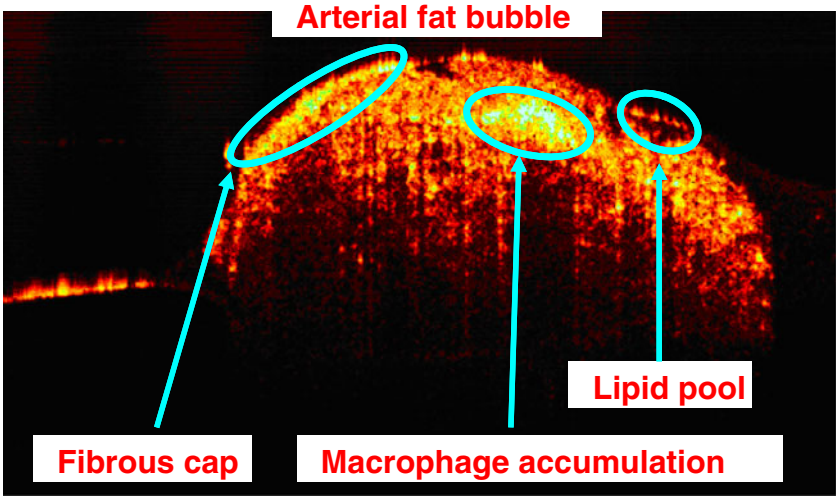

Fig. 6 OCT image of a fatty bubble located on the luminal side of an arterial sample harvested from a WHHL-MI rabbit. Structures such as macrophage accumulations, lipid pools and fibrous caps are evident in the image

provide enhanced structural information. Caries lesion depths measured non-invasively by OCT are comparable to the results obtained by gold-standard destructive methods such as histology and microradiography, for determining lesion depth (Choo-Smith et al. 2008). OCT is therefore able to provide morphological information of near-surface tissue structures and defects in the tooth and is particularly sensitive to changes in refractive index as the light interacts with the sample. The method shows promise for use in screening for early dental caries which go largely undetected by X-ray examination. OCT can also be used for estimating the lesion depth and extent of tooth surface demineralization without the need for ionizing radiation (Popescu et al. 2008). From a clinical perspective, it can be useful for determining the extent of caries activity and in aiding the decision either to restore or to promote re-mineralization. In addition, OCT measurements of teeth at regular intervals can be used to demonstrate whether the caries process has been arrested and to monitor the effectiveness of re-mineralization treatments. As an example, a demineralized portion of dental tissue is demonstrated in the OCT image of a tooth acquired at 830 nm (Fig. 7). This B-scan contains 100 A-scans and corresponds to dental tissue that is 2 mm wide and ~1.2 mm deep. The demineralized tissue is on the left side of the image while a small portion of healthy tissue is localized on its right side. Demineralization leads to OCT signal being recorded from deeper within the dental matrix when compared to the depth penetrated by OCT signal in healthy tissue. The depth and extension of such lesions, also called "white spots", can be easily determined by OCT imaging but not through X-ray.

As a clinical specialty, gastroenterology uses white-light endoscopy to visually examine organs responsible for digestion. It is known that most of the cancers of the gastrointestinal tract arise in the outer most layers of the tissue, the mucosa. Therefore, the ability to accurately assess the status of this layer is imperative. Although there have been many efforts to improve endoscopic diagnosis and move away from solely from visual inspection, only endoscopic ultrasonography (EUS) has clinically become established. However, its resolution is insufficient for probing the mucosal layers in detail. The shortcomings of EUS include: high cost, the necessity to evaluate a large number of biopsies, low yield, delayed diagnosis and, the most serious of all, the sampling error where dysplasia and early cancer can be overlooked (Falk et al. 1999). Due to its higher spatial resolution and ability to image structures located underneath a surface, endoscopic OCT is well suited to make the greatest clinical impact in the diagnosis of various disorders affecting the mucosa. Izatt et al. 1996 demonstrated that OCT can clearly delineate the individual layers of the mucosa and differentiate mucosa from submucosa in stomach and colon. Also, OCT images showed obvious differences between normal and malignant tissue in human esophagus, stomach, small intestine and colon (Tearney et al. 1997; Kobayashi et al. 1998). In addition, Boppart et al. (1999) used excised rat tissue to study the feasibility of OCT-guided photoablative argon laser therapy. Their results suggested that OCT imaging can also be used for monitoring the therapy. Assessing the state of muscularis mucosae (deepest layer of the mucosa) is necessary when determining the malignancy invasiveness, and a study has shown that the thickness of this layer can be imaged by OCT (Cilesiz et al. 2002). Ex vivo studies conducted by Westphal et al. (2005) proved the perfect correlation between OCT images and their corresponding histology samples. Das et al. (2001) demonstrated that catheter probe OCT and EUS are complementary rather than competing technologies. The depth of penetration of OCT is insufficient for evaluating the deeper layers (muscularis propria) but, due to its micrometer resolution, it is excellent for diagnosis of the mucosa and submucosa layers.

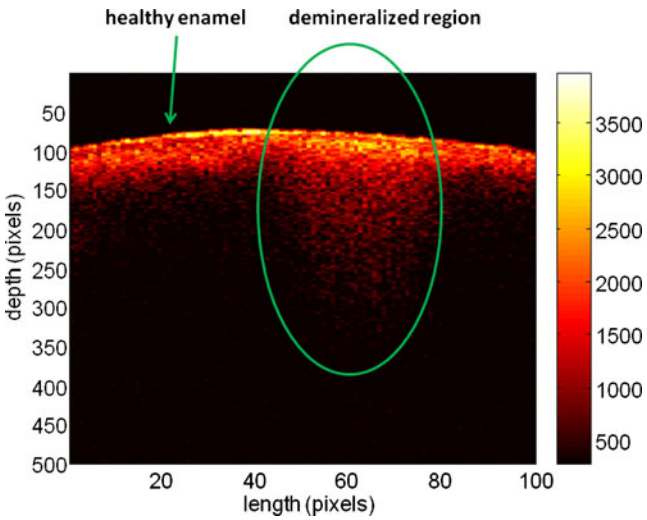

Fig. 7 OCT image of a tooth containing both healthy and demineralized tissue

Conclusion

This review paper provides a brief overview of some of the main technical aspects of optical coherence tomography (OCT) for the reader who is not very familiar with this technology and wants to obtain a quick glimpse at the potential and challenges of this imaging method. OCT is a light interference-based imaging technology that has made huge strides in biomedical research and medicine in the last decade. Its main strength is the capability of real-time in situ 3D visualization of tissue structure and pathology

without the need to excise and process the sample tissue. It provides images with a spatial resolution of micrometers and with the possibility to detect structures located at depths of millimeters underneath the surfaces of probed tissues. OCT has had the most clinical impact in ophthalmology, where it provides quantitative information that cannot be obtained by any other imaging method. Fiber-based OCT systems can be easily interfaced with a wide range of instruments such as catheters, laparoscopes or endoscopes, thus enabling the imaging of internal organs systems: arterial, intestinal, digestive, pulmonary, etc. By now, tremendous progress has been achieved in intravascular OCT imaging, with the method being approved in over 35 countries for clinical use to obtain real-time images of coronary arteries during cardiology interventions. As a tool for fundamental research, OCT has a broad spectrum of applications in small animal imaging, developmental biology, tissue engineering and the development of new biocompatible materials. From the technological angle, the advances in Fourier-domain OCT had a huge impact, ensuring tremendous data acquisition speeds thus allowing in vivo acquisition of 3D-OCT volumetric data and signal averaging techniques that offer measurements of unmatched sensitivity. The incessant innovation process on going in OCT imaging technology all over the world will undoubtedly open new applications for this method in clinical medicine and in fundamental biomedical research.

References

Akiba M, Chan KP, Tanno N (2003) Full-field optical coherence tomography by two- dimensional heterodyne detection with a pair of CCD cameras. Opt Lett 28:816–818

Amaechi BT, Higham SM, Podoleanu AG, Rogers JA, Jackson DA (2001) Use of optical coherence tomography for assessment of dental caries: quantitative procedure. J Oral Rehabil 28:1092–1093

Amaechi BT, Podoleanu A, Higham SM, Jackson DA (2003) Correlation of quantitative light-induced fluorescence and optical coherence tomography applied for detection and quantification of early dental caries. J Biomed Opt 8:642–647

Baumgartner A, Dichtl S, Hitzenberger CK, Sattmann H, Robl B, Moritz A, Fercher AF, Sperr W (2000) Polarization-sensitive optical coherence tomography of dental structures. Caries Res 34:59–69

Brandenburg R, Haller B, Hauger C (2003) Real-time in vivo imaging of dental tissue by means of optical coherence tomography (OCT). Opt Commun 227:203–211

Bonnema GT, Cardinal KO, Williams SK, Barton JK (2009) A concentric three element radial scanning optical coherence tomography endoscope. J Biophoton 2:353–356

Boppart SA, Herrmann J, Pitris C, Stamper DL, Brezinski ME, Fujimoto JG (1999) High- resolution optical coherence tomography-guided laser ablation of surgical tissue. J Surg Res 82:275–284

Chang S, Liu X, Cai X, Grover CP (2005) Full-field optical coherence tomography and its application to multiple-layer 2D information retrieving. Opt Comm 246:579–585

Chang S, Cai X, Flueraru C (2007) An efficient algorithm used for full-field optical coherence tomography. Opt Lasers Eng 45:1170–1176

Chang S, Murdock E, Mao Y, Flueraru C (2010) Optical catheter with rotary optical cap. US patent 662:447

Chinn SR, Swanson EA, Fujimoto JG (1997) Optical coherence tomography using a frequency-tunable optical source. Opt Lett 22:340–342

Choma MA, Sarunic MV, Yang C, Izatt JA (2003) Sensitivity advantage of swept source and fourier domain optical coherence tomography. Opt Expr 11:2183–2189

Choo-Smith LP, Qiu P, Popescu DP, Hewko M, Dong CCS, Cleghorn BM, Sowa MG (2008) Determining depths of incipient caries from OCT imaging. J Dent Res 87(Spec Iss B):2838

Cilesiz L, Fockens P, Kerindongo R, Faber D, Tytgat G, Kate FT, Leuwen TV (2002) Comparative optical coherence tomography imaging of human esophagus: How accurate is localization of the muscularis mucosae? Gastrointest Endosc 56:852–857

Colston BW Jr, Everett MJ, Sathyam US, DaSilva LB, Otis LL (2000) Imaging of the oral cavity using optical coherence tomography. Monogr Oral Sci 17:32–55

Das A, Sivak MV Jr, Chak A, Wong RC, Westphal V, Rollins AM, Willis J, Isenberg G, Izatt JA (2001) High-resolution endoscopic imaging of the GI tract: A comparative study of optical coherence tomography versus high-frequency catheter probe EUS. Gastrointest Endosc 54:219–224

Dolin LS (1998) A theory of optical coherence tomography. Radiophys Quant Electron 41:850–873

Dubois A (2001) Phase-map measurements by interferometry with sinusoidal phase modulation and four integrating buckets. J Opt Soc Am A 18:1972–1979

Dubois A (2004) Effects of phase change on reflection in phase-measuring interference microscopy. Appl Opt 43:1503–1507

Dubois A, Vabre L, Boccara AC, Beaurepaire E (2002) High-resolution ful-field optical coherence tomography with a Linnik microscope. Appl Opt 41:805–812

Falk GW, Rice TW, Goldblum JR, Richter JE (1999) Jumbo biopsy forceps protocol still misses unsuspected cancer in Barrett's esophagus with high-grade dysplasia. Gastrointest Endosc 49:170–176

Feldchtein F, Gelikonov V, Iksanov R, Gelikonov G, Kuranov R, Sergeev A, Gladkova N, Ourutina M, Reitz D, Warren J (1998) In vivo OCT imaging of hard and soft tissue of the oral cavity. Opt Express 3:239–250

Fercher AF (1996) Optical coherence tomography. J Biomed Opt 1:157–173

Fercher AF, Roth E (1986) Opthalmic laser interferometry. Proc SPIE 658:48–51

Fercher AF, Mengedoht K, Werner W (1988) Eye-length measurement by interferometry with partially coherent light. Opt Lett 13:186–188

Fercher FA, Hitzenberger CK, Drexler W, Kemp G, Sattman H (1993) In vivo optical coherence tomography. Am J Ophthalmol 116:113–114

Fercher AF, Hitzenberger CK, Kamp G, Elzaiat SY (1995) Measurement of intraocular distances by backscattering spectral interferometry. Opt Comm 117:43–48

Flueraru C, Popescu DP, Mao Y, Chang S, Sowa MG (2010) Added soft tissue contrast using the signal attenuation and the fractal dimension for optical coherence tomography images of porcine arterial tissue. Phys Med Biol 55:2317–2331

Fried D, Xie J, Shafi S, Featherstone JDB, Breunig TM, Le C (2002) Imaging caries and lesion progression with polarization sensitive optical coherence tomography. J Biomed Opt 7:618–627

Fried D, Featherstone JD, Darling CL, Jones RS, Ngaotheppitak P, Buhler CM (2005) Early caries imaging and monitoring with near-infrared light. Dent Clin North Am 49:771–793

Fujimoto JG, De Silvestri S, Ippen EP, Puliafito CA, Margolis R, Oseroff A (1986) Femtosecond optical ranging in biological systems. Opt Lett 11:150–152

Goldberg BD, Iftimia NV, Bressner JE, Pitman MB, Halpern E, Bouma BE, Tearney GJ (2008) Automated algorithm for differentiation of human breast tissue using low coherence interferometry for fine needle aspiration biopsy guidance. J Biomed Opt 13:014014

Golubovic B, Bouma BE, Tearney GJ, Fujimoto JG (1997) Optical frequency-domain reflectometry using rapid wavelength tuning of a Cr4+:Forsterite laser. Opt Lett 22:1704–1706

Greivenkamp JE, Bruning JH (1992) Phase shift interferometers. In: Optical Shop Testing, 2nd edn. Wiley, New York, pp 501–598

Hausler G, Lindner MW (1998) "Coherence radar" and "spectral radar" - new tools for dermatological diagnosis. J Biomed Opt 3:21–31

Herz PR, Chen Y, Aguirre AD, Schneider K, Hsiung P (2004) Micromotor endoscope catheter for in vivo, ultrahigh-resolution optical coherence tomography. Opt Lett 29:2261–2263

Hitzenberger C, Goetzinger E, Sticker M, Pircher M, Fercher A (2001) Measurement and imaging of birefringence and optic axis orientation by phase resolved polarization sensitive optical coherence tomography. Opt Express 9:780–790

Huang D, Swanson EA, Lin CP, Schuman JS, Stinson WG, Chang W, Hee MR, Flotte T, Gregory K, Puliafito CA, Fujimoto JG (1991) Optical coherence tomography. Science 254:1178–1181

Iftimia NV, Bouma BE, Pitman MB, Goldberg B, Bressner J, Tearney GJ (2005) A portable, low coherence interferometry based instrument for fine needle aspiration biopsy guidance. Rev Sci Instrum 76:064301

Isenberg G, Sivak MV, Chak A, Wong RCK, Willis JE, Wolf B, Rowland DY, Das A, Rollins A (2005) Accuracy of endoscopic optical coherence tomography in the detection of dysplasia in Barrett's esophagus: a prospective, double-blinded study. Gastrointest Endosc 62:825–831

Izatt JA, Hee MR, Owen GM, Swanson EA, Fujimoto JG (1994) Optical coherence microscopy in scattering media. Opt Lett 19:590–592

Izatt JA, Kulkarni MD, Wang HW, Kobayashi K, Sivak MV Jr (1996) Optical coherence tomography and microscopy in gastrointestinal tissues. IEEE J Sel Top Quant Electron 2:1017–1028

Jafri MS, Farhang S, Tang RS, Desai N, Fishman PS, Rohwer RG, Tang C, Schmitt JM (2005) Optical coherence tomography in the diagnosis and treatment of neurological disorders. J Biomed Opt 10:051603

Jang IK, Hursting MJ (2005) When heparins promote thrombosis: review of heparin- induced thrombocytopenia. Circulation 111:2671–2683

Jang IK, Tearney GJ, Bouma BE (2001) Visualization of tissue prolapsed between coronary stent struts by optical coherence tomography: comparison with intravascular ultrasound. Circulation 104:2754

Jang IK, Bouma BE, Kang DH, Park SJ, Park SW, Seung KB, Choi KB, Shishkov M, Schlendorf K, Pomerantsev E, Houser SL, Aretz HT, Tearney GJ (2002) Visualization of coronary atherosclerotic plaques in patients using optical coherence tomography: comparison with intravascular ultrasound. J Am Coll Cardiol 39:604–609

Kino GS, Chim SC (1990) Mirau correlation microscope. Appl Opt 29:3775–3783

Kobayashi K, Izatt JA, Kulkarni MD, Willis J, Sivak MV Jr (1998) High-resolution cross-sectional imaging of the gastrointestinal tract using optical coherence tomography. Preliminary results. Gastrointest Endosc 47:515–523

Leitgeb R, Hitzenberger CK, Fercher AF (2003) Performance of Fourier domain vs. time domain optical coherence tomography. Opt Exp 11:889–894

Lexer F, Hitzenberger CK, Fercher AF, Kulhavy M (1997) Wavelength-tuning interferometry of intraocular distances. Appl Opt 36:6548–6553

Li H, Standish BA, Mariampillai A, Munce NR, Mao Y, Chiu S, Marcon NE, Wilson BC, Vitkin A, Yang VXD (2006) Feasibility of interstitial Doppler optical coherence tomography for in vivo detection of microvascular changes during photodynamic therapy. Lasers Surg Med 38:754–761

Liu X, Cobb MJ, Chen Y, Kimmey MB, Li X (2004) Rapid-scanning forward-imaging miniature endoscope for real-time optical coherence tomography. Opt Lett 29:1763–1765

Mao Y, Chang S, Sherif S, Flueraru C (2007) Graded-index fiber lens proposed for ultrasmall probes used in biomedical imaging. Appl Opt 46:5887–5894

Mao Y, Chang S, Flueraru C (2010) Fiber lenses for ultra-small probes used in optical coherent tomography. J Biomed Sci Eng 3:27–34

Maragos P, Kaiser JF, Quatieri TF (1993) On amplitude and frequency demodulation using energy operators. IEEE Trans Signal Process 41:1532–1550

Min EJ, Na J, Ryu SY, Lee BH (2009) Single-body lensed-fiber scanning probe actuated by magnetic force for optical imaging. Opt Lett 34:1897–1899

Morkel PR, Laming R, Payne DN (1990) Noise characteristics of high-power doped-fiber superluminescent sources. Electron Lett 26:96–97

Munce NR, Yang VXD, Standish B, Qiang B, Mao Y, Li H, Butany J, Courtney BK, Graham JJ, Dick AJ, Strauss BH, Wright GA, Vitkin IA (2006) Ex vivo imaging of chronic total occlusions using forward-looking optical coherence tomography. Lasers Surg Med 39:28–35

Munce NR, Mariampillai A, Standish BA, Pop M, Anderson KJ, Liu GY, Luk T, Courtney BK, Wright GA, Vitkin IA, Yang VXD (2008) Electrostatic forward- viewing scanning probe for Doppler optical coherence tomography using a dissipative polymer catheter. Opt Lett 33:657–659

Murphy E (2008) The Evolution of Spectral Domain OCT. http://www.ophmanagement.com/article.aspx?article=101888

Ngaotheppitak P, Darling CL, Fried D (2005) Measurement of the severity of natural smooth surface (interproximal) caries lesions with polarization sensitive optical coherence tomography. Lasers Surg Med 37:78–88

Novak J (2003) Five-step phase-shifting algorithms with unknown values of phase shift. Optik-Intl Light Electr Opt 114:63–68

Oliver BM (1965) Thermal and quantum noise. Proc IEEE 53:436–454

Takada K (1998) Noise in optical low coherence reflectometry. IEEE J Quant Elect 34:1098–1108

Pan Y, Birngruber R, Rosperich J, Engelhardt R (1995) Low-coherence optical tomography in turbid tissue: theoretical analysis. Appl Opt 34:6564–6574

Patel NA, Stamper DL, Brezinski ME (2005) Review of the ability of optical coherence tomography to characterize plaque, including a comparison with intravascular ultrasound. Cardiovasc Intervent Radiol 28:1–9

Petersen CL, McNamara EI, Lamport RB, Atlas M, Schmitt JM, Swanson EA, Magnin P (2005) Scanning miniature optical probes with optical distortion correction and rotational control. US Patent, 6891984

Podoleanu AG (2000) Unbalanced versus balanced operation in an optical coherence tomography system. Appl Opt 39:173–182

Podoleanu AG, Jackson DA (1999) Noise analysis of a combined optical coherence tomography and a confocal scanning ophthalmoscope. Appl Opt 38:2116–2127

Popescu DP, Sowa MG, Hewko MD, Choo-Smith L-P (2008) Assessment of early demineralization in teeth using the signal attenuation in optical coherence tomography images. J Biomed Opt 13:054053. doi:10.1117/1.2992129

Popescu DP, Flueraru C, Mao Y, Chang S, Sowa MG (2010) Signal attenuation and box- counting fractal analysis of optical coherence images of arterial tissue. Biomed Opt Express 1:268–277

Reed WA, Yan MF, Schnitzer MJ (2002) Gradient-index fiber-optic microprobes for minimally invasive in vivo low-coherence interferometry. Opt Lett 27:1794–1796

Regar E, Schaar JA, Mont E, Virmani R, Serruys PW (2003) Optical coherence tomography. Cardiovasc Radiat Med 4:198–204

Rollins AM, Izatt JA (1999) Optical interferometer designs for optical coherence tomography. Opt Lett 24:1484–1486

Rosa CC, Podoleanu AG (2004) Limitation to the achievable signal to noise ratio in optical coherence tomography due to mismatch of the balanced receiver. Appl Opt 43:4802–4815

Saleh B (1978) Photoelectron statistics. Springer-Verlag, Berlin

Schmitt JM (1999) Optical coherence tomography (OCT): A review. IEEE J Sel Top Quant Electron 5:1205–1215

Schmitt JM, Knuttel A, Yadlowsky AM, Eckhaus MA (1994) Optical-coherence tomography of a dense tissue: statistics of attenuation and backscattering. Phys Med Biol 39:1705–1720

Sherif SS, Rosa CC, Flueraru C, Chang S, Mao Y, Podoleanu AG (2008) Statistics of the depth-scan photocurrent in time-domain optical coherence tomography. J Opt Soc Am 25:16–20

Shiomi M, Ito T, Yamada S, Kawashima S, Fan J (2003) Development of an Animal Model for Spontaneous Myocardial Infarction (WHHL-MI Rabbit). Arterioscler Thromb Vasc Biol 23:1239–1244

Shishkov M, Bouma BE, Jang IK, Jang DH, Aretz HT, Houser SL, Brady TJ, Schlendorf K, Tearney GJ (2000) Optical coherence tomography of porcine coronary arteries in vivo. Presented at the 2000 Optical Society of America Biomedical Topical Meeting, Miami, Florida

Shishkov M., Bouma BE, Tearney GJ (2006) System and method for optical coherence tomography. US Patent, 20060067620A1

Smolka G (2008), Optical Coherence Tomography – Technology, Markets, and Applications 2008–2012, BioOptics World – PenWell Corp., www.BioOpticsWorld.com/resourcecenter/OCTreport.html

Standish B, Yang V, Munce N, Song L, Gardiner G, Lin A, Mao Y, Vitkin A, Marcon N, Wilson B (2007) Doppler optical coherence tomography monitoring of microvascular tissue response during photodynamic therapy in an animal model of Barrett's esophagus. Gastrointest Endosc 66:326–333

Strategies Unlimited, Optical Coherence Tomography (2010) Technology, Applications, and Market, January 2010 at http://www.optoiq.com/index/market-research/display/su-article-display/articles/strategies-unlimited/reports/2010/1/optical-coherence.html

Su J, Zhang J, Yu L, Chen Z (2007) In vivo three-dimensional microelectromechanical endoscopic swept source optical coherence tomography. Opt Express 15:10390–10396

Swanson EA, Huang D, Hee MR, Fujimoto JG, Lin CP, Puliafito CA (1992) High-speed optical coherence domain reflectometry. Opt Lett 17:151–153

Swanson EA, Izatt JA, Hee MR, Huang D, Lin CP, Schuman JS, Puliafito CA, Fujimoto JG (1993) In vivo retinal imaging by optical coherence tomography. Opt Lett 18:1864–1869

Swanson E, Petersen CL, McNamara E, Lamport RB, Kelly DL (2002) Ultra-small optical probes, imaging optics, and methods for using same. US Patent, 6445939

Takahashi Y, Iwaya M, Watanabe Y, Sato M (2007) Optical probe using eccentric optics for optical coherence tomography. Opt Commun 271:285–290

Tearney GJ, Brezinski ME, Southern JF, Bouma BE, Boppart SA, Fujimoto JG (1997) Optical biopsy in human gastrointestinal tissue using optical coherence tomography. Am J Gastro 92:1800–1804

Tearney GJ, Jang IK, Bouma BE (2003a) Evidence of cholesterol crystals in atherosclerotic plaque by optical coherence tomographic (OCT) imaging. Eur Heart J 24:1462–1467

Tearney GJ, Yabushita H, Houser SL, Aretz HT, Jang IK, Schlendorf K, Kauffmann CR, Shishkov M, Halpern EF, Bouma BE (2003b) Quantification of macrophage content in atherosclerotic plaques by optical coherence tomography. Circulation 107:113–119

Tran PH, Mukai DS, Brenner M, Chen Z (2004) In vivo endoscopic optical coherence tomography by use of a rotational microelectromechanical system probe. Opt Lett 29:1236–1238

Vabre L, Dubois A, Boccara AC (2002) Thermal-light full-filed optical coherence tomography. Opt Lett 27:530–532

Van der Meer FJ, Faber DJ, Sassoon DMB, Aalders MC, Pasterkamp G, Van Leeuwen TG (2005) Localized measurement of optical attenuation coefficients of atherosclerotic plaque constituents by quantitative optical coherence tomography. IEEE Trans Med Imaging 24:1369–1376

Walz M (2006) Hot Technologies for 2007: OCT: Imaging of the Future. R&D Mag 6. http://www.rdmag.com/Featured-Articles/2006/12/Hot-Technologies-for-2007-OCT-Imaging-of-the-Future/

Wang XJ, Milner TE, de Boer JF, Zhang Y, Pashley DH, Nelson JS (1999) Characterization of dentin and enamel by use of optical coherence tomography. Appl Opt 38:2092–2096

Wang ZG, Lee CSD, Waltzer WC, Liu JX, Xie HK, Yuan ZJ, Pan YT (2007) In vivo bladder imaging with microelectromechanical systems-based endoscopic spectral domain optical coherence tomography. J Biomed Opt 12:034009

Wang J, Hathaway M, Shidlovski V, Dainty C, Podoleanu A (2009) Evaluation of the signal noise ratio enhancement of SS-OCT versus TD-OCT using a full field interferometer. Proc SPIE 7168:71682K. doi:10.1117/12.809043

Westphal V, Rollins AM, Willis J, Sivak MV Jr, Izatt JA (2005) Correlation of endoscopic optical coherence tomography with histology in the lower-GI tract. Gastrointest Endosc 61:537–546

Wojtkowski M, Leitgeb R, Kowalczyk A, Bajraszewski T, Fercher AF (2002) In vivo human retinal imaging by fourier domain optical coherence tomography. J Biomed Opt 7:457–463

Wu L, Xie H (2009) Electrothermal micromirror with dual-reflective surfaces for circumferential scanning endoscopic imaging. J Micro/Nanolith MEMS MOEMS 8:013030. doi:10.1117/1.3082186

Wu J, Conry M, Gu C, Wang F, Yaqoob Z, Yang C (2006) Paired-angle-rotation scanning optical coherence tomography forward-imaging probe. Opt Lett 31:1265–1267

Xu Y, Singh J, Jason THS, Ramakrishna K, Premchandran CS, Kelvin CWS, Kuan CT, Chen M, Olivo MC, Sheppard CJR (2007) MEMS based non-rotatory circumferential scanning optical probe for endoscopic optical coherence tomography Proc SPIE 6627:662715. doi:10.1117/12.726736

Yabushita H, Bouma BE, Houser SL, Aretz HT, Jang IK, Schlendorf KH, Kauffmann CR, Shishkov M, Kang DH, Halpern EF, Tearney GJ (2002) Characterization of human atherosclerosis by optical coherence tomography. Circulation 106:1640–1645

Yang VXD, Mao YX, Munce N, Standish B, Kucharczyk W, Marcon NE, Wilson BC, Vitkin IA (2005) Interstitial doppler optical coherence tomography. Opt Lett 30:1791–1793

Zara JM, Patterson PE (2006) Polyimide amplified piezoelectric scanning mirror for spectral domain optical coherence tomography. Appl Phys Lett 89:263901. doi:10.1063/1.2410239